European Cells and Materials Vol. 44 2022 (pages 115-132) DOI: 10.22203/eCM.v044a08 ISSN 1473-2262

PRENATAL MURINE SKELETOGENESIS PARTIALLY RECOVERS FROM ABSENT SKELETAL MUSCLE AS DEVELOPMENT PROGRESSES

V. Sotiriou[1], Y. Huang[1], S. Ahmed[1], H. Isaksson[2] and N.C. Nowlan[1,3,4,*]

[1] Department of Bioengineering, Imperial College London, London SW7 2AZ, UK
[2] Department of Biomedical Engineering, Lund University, Box 118, 221 00 Lund, Sweden
[3] School of Mechanical and Materials Engineering, University College Dublin, Dublin 4, Ireland
[4] Conway Institute, University College Dublin, Dublin 4, Ireland

Abstract

Skeletal muscle contractions are critical for normal skeletal growth and morphogenesis but it is unclear how the detrimental effects of absent muscle on the bones and joints change over time. Joint shape and cavitation as well as rudiment length and mineralisation were assessed in multiple rudiments at two developmental stages [Theiler stage (TS)24 and TS27] in the splotch-delayed "muscle-less limb" mouse model and littermate controls. Chondrocyte morphology was quantified in 3D in the distal humerus at the same stages. As development progressed, the effects of absent muscle on all parameters except for cavitation become less severe. All major joints in muscle-less limbs were abnormally shaped at TS24, while, by TS27, most muscle-less limb joint shapes were normal or nearly normal. In contrast, any joints that were fused at TS24 did not cavitate by TS27. At TS24, chondrocytes in the distal humerus were significantly smaller in the muscle-less limbs than in controls, while by TS27, chondrocyte volume was similar between the two groups, offering a cell-level mechanism for the partial recovery in shape of muscle-less limbs. Mineralisation showed the most pronounced changes over gestation. At TS24, all muscle-less rudiments studied had less mineralisation than the controls, while at TS27, muscle-less limb rudiments had mineralisation extents equivalent to controls. In conclusion, the effects of muscle absence on prenatal murine skeletogenesis reduced in severity over gestation. Understanding how mammalian bones and joints continue to develop in an environment with abnormal fetal movements provides insights into conditions including hip dysplasia and arthrogryposis.

Keywords: Prenatal skeletal development, fetal movements, developmental biomechanics, cartilage, bone, morphogenesis, ossification, mouse.

***Address for correspondence**: Prof. Niamh C. Nowlan, School of Mechanical and Materials Engineering, University College Dublin (UCD), Dublin 4, Ireland.
Email: niamh.nowlan@ucd.ie

List of Abbreviations

ANOVA	analysis of variance
BABB	benzyl alcohol/benzyl benzoate
ECM	extracellular matrix
Pax3	paired box 3
PCR	polymerase chain reaction
PFA	paraformaldehyde
OCT	optimal cutting temperature
OPT	optical projection tomography
Sp^d	Splotch delayed
TS	Theiler stage

Introduction

Fetal movements play an important role in prenatal skeletal development (Nowlan, 2015). When the skeletal muscle in animal models is absent, reduced in volume or non-contractile, skeletal rudiments tend to be shorter, with decreased mineralisation and malformed joints (Bridglal *et al.*, 2021; Brunt *et al.*, 2016; Kahn *et al.*, 2009; Khatib *et al.*, 2021; Nowlan *et al.*, 2008; Nowlan *et al.*, 2010; Nowlan *et al.*, 2014; Pierantoni *et al.*, 2021; Roddy *et al.*, 2011; Sotiriou *et al.*, 2019). Vertebral segmentation, vertebral shape and intervertebral disc formation are also dependent on muscle forces (Levillain *et al.*, 2019; Levillain *et al.*, 2021; Rolfe *et al.*, 2017). Not all bones are affected equally by compromised skeletal muscles, with the bones and joints of the forelimb being more severely affected than those of the hindlimb (Kahn *et al.*, 2009; Nowlan *et al.*, 2010; Sotiriou *et al.*, 2019). Unequal stimulation of the muscle-less limbs from passive movements has been proposed as a possible mechanism underlying the differential effects of

absent muscle on skeletal development (Nowlan *et al.*, 2012). While skeletal muscle contractions are critical for normal growth and morphogenesis of most bones in the limbs and spine, the effects of abnormal skeletal muscle on mammalian skeletal development over time *in utero* have not been characterised in detail.

Few studies have investigated the temporal effects of mechanical forces due to skeletal muscle contractions over development. Very early stages of skeletal development occur independently of skeletal muscle contractions, including interzone formation (Kahn *et al.*, 2009; Mikic *et al.*, 2000), joint morphogenesis prior to cavitation (Nowlan and Sharpe, 2014) and notochord involution (Levillain *et al.*, 2021). Bridglal *et al.* (2021) have recently shown that the time window between embryonic days 4 and 7 is the most important period for muscle forces in terms of the effects on hip-joint development in the chick embryo, but the effects of immobilisation do not become pronounced until day 8 and later (Nowlan *et al.*, 2014). Also, in the chick embryo, a single day of immobilisation at embryonic days 3 or 4 has pronounced, lasting effects on spinal curvature, vertebral segmentation and vertebral shape, while single-day immobilisation at embryonic day 5 leads to the most severe rib abnormalities (Levillain *et al.*, 2019). Pollard *et al.* (2017) found that the area of the furcula (part of the pectoral girdle in birds) was unchanged by short period of flaccid paralysis but significantly reduced by sustained flaccid paralysis between embryonic days 10 and 18. Drachman and Coulombre (1962) reported relatively severe effects on the skeleton at hatching after 1 or 2 d of paralysis between 7 and 9 d of incubation, indicating that the effects of temporary paralysis (at least in the chick) may become more severe as development progresses. Most published works considering a temporal component use the chick or fish model system and only a few studies using mammalian model systems assess the effects of absent or abnormal muscle upon skeletal development over time (Kahn *et al.*, 2009; Pierantoni *et al.*, 2021). Kahn *et al.* (2009) assessed joint development in mice with absent or non-contractile skeletal muscle at multiple developmental stages [embryonic day (e)12.5, 13.5, 14.5, 16.5 and 18.5] and reported that elbow joint fusion, first detectable at e16.5 (~ TS25), is maintained until e18.5 (equivalent to TS27). Joint shape was not quantitatively assessed. Pierantoni *et al.* (2021) quantified humeral bone properties, including bone volume and extent at TS23, TS24 and TS27, in muscle-less limb and control embryos and reported that while many mineralisation parameters were significantly different between musclele-less and controls at TS24, mineralisation had caught up in the muscle-less limb humeri by TS27. Temporal characterisation of the effects of muscle absence on rudiments other than the humerus are lacking and the progression of joint shape in the absence of skeletal muscle has not been quantified. Given the known differential effects of absent or abnormal muscles on different skeletal rudiments (Kahn *et al.*, 2009; Nowlan *et al.*, 2010), a holistic study of the effects of muscle absence on all key aspects of the developing mammalian skeleton is warranted.

In the present work, the progression of prenatal skeletal development when skeletal muscles are absent was investigated, to determine if the effects on the bones and joints remained constant, worsen or improved over developmental time. Understanding the temporal effects of intra-uterine immobility has impact for conditions such as amyoplasia and developmental dysplasia of the hip, in which an early, often temporary, period of restricted or reduced movement can have long-lasting consequences on joint shape (Nowlan, 2015). Key parameters of skeletal development were assessed, namely joint size, shape and cavitation as well as rudiment length and mineralisation, for multiple rudiments and over two developmental stages, TS24 (e15.5) and TS27 (e18.5), in the splotch-delayed muscle-less limb mouse model and littermate controls. 3D data were obtained using OPT, followed by rigid image registration, to characterise morphology, and histology was used for assessment of cavitation. Finally, the cell-level events underlying the temporal effects of absent skeletal muscles on joint development were explored. Muscle-less limbs and littermate control limbs at TS24 and TS27 were imaged using high resolution phase-contrast synchrotron X-ray tomography. Matrix proportion, chondrocyte volume as well as chondrocyte orientation in the distal humerus were compared between groups.

Material and Methods

Animal model

All animal experiments were performed in accordance with the European legislation (Directive 2010/63/EU). Embryos from the *Pax3*$^{Sp/Sp}$ (Sp^{d}) mice were studied. In *Pax3* mutants, muscle progenitor cells do not migrate to the limb buds and, thus, the limbs are devoid of skeletal muscles (Franz *et al.*, 1993). Homozygous mutations in *Pax3* are neonatal lethal, while heterozygous embryos have no limb muscle abnormalities (Franz *et al.*, 1993). Heterozygous adult animals were imported from The Jackson Laboratory (JAX stock #000565) and interbred. Pregnant mice were sacrificed using cervical dislocation and embryos were euthanised and staged according to Theiler's Staging criteria (Theiler, 1989). Genotyping was done by PCR on DNA derived from head tissue. The PCR reaction was carried out for 30 cycles, each with a duration of 30 s each at 94, 60 and 74 °C, using three primers. Primer sequences used were AGGGCCGAGTCAACCAGCACG and CACGCGAAGCTGGCGAGAAATG for controls and AGTGTCCACCCCTCTTGG-CCTCGGCCGAGTCAACCAGGTCC and CACGCGAAGCTGGCGAGAAATG for mutants. For the organ-level morphological analyses, five muscle-

less and littermate control embryos at TS24 and at TS27 were analysed in detail. The control embryos came from one (TS24) or two (TS27) litters, while the muscle-less limb embryos came from two (TS24) or three (TS27) litters. TS24 (around e15.5) was chosen as a stage distinct from TS23, which has already been characterised in detail (Nowlan *et al.*, 2010; Sotiriou *et al.*, 2019), and TS27 (around e18.5) was chosen as it is the latest reliably obtainable stage the embryos reach just before birth. 4 animals per group and stage were analysed for chondrocyte morphology using high-resolution phase-contrast synchrotron X-ray tomography.

3D optical projection tomography and image registration

Left forelimbs and hindlimbs were dehydrated and stained for cartilage and mineralised tissue using alcian blue and alizarin red S, as previously described (Sotiriou *et al.*, 2019). Stained and fixed limbs were embedded in agarose, dehydrated and cleared in a solution of BABB in preparation for 3D imaging using OPT, according to Quintana and Sharpe (2011). Limbs were scanned under visible light to obtain 3D images of the alcian blue staining (cartilage) and under the Texas-red filter to obtain auto-fluorescent 3D images of the alizarin red S-stained region (the mineralised region). Scans were reconstructed using NRecon (SkyScan, Bruker microCT, 2011). Segmentation of the cartilaginous scapula, humerus, ulna, radius, pelvis, femur and tibia was performed using Mimics (v17.0, Materialise, Leuven, Belgium). The fibula was prone to deformation and twisting, making it difficult to reliably segment it and, therefore, was not included in any analyses. As previously described (Sotiriou *et al.*, 2019), segmentation was still possible when rudiments were fused, due to the joint line being still identifiable based on reduced intensity of staining. Segmented rudiments were prepared for image registration using TransformJ (Meijering *et al.*, 2001) in ImageJ (Schneider *et al.*, 2012), being first roughly aligned with other rudiments of the same type, scaled to a consistent magnification and allocated the same canvas area. Image brightness was normalised using Matlab (version R2015a, the MathWorks, Inc.). The Image Registration Toolkit software (Schnabel *et al.*, 2001) (IRTK, BioMedia, Imperial College London, London, UK) was used to align rudiments to each other, with rigid registration, as previously described (Sotiriou *et al.*, 2019). A robust process of alignment of all datasets in 3D facilitated repeatable and reliable measurements of complex 3D shapes. Segmentation or image registration were not necessary for the alizarin red S scans, due to the simple nature of the bone collar measurements taken.

Measurements and statistics

For joint shape characterisation, the same set of 25 forelimb measurements and 27 hindlimb measurements described in a previous study of muscle-less limb joint shapes at TS23 were used, as reproduced in Fig. 1,2 (with permission). Consistent measurements were made from equivalent sections and planes of each individual rudiment by applying the same rotations to each registered rudiment

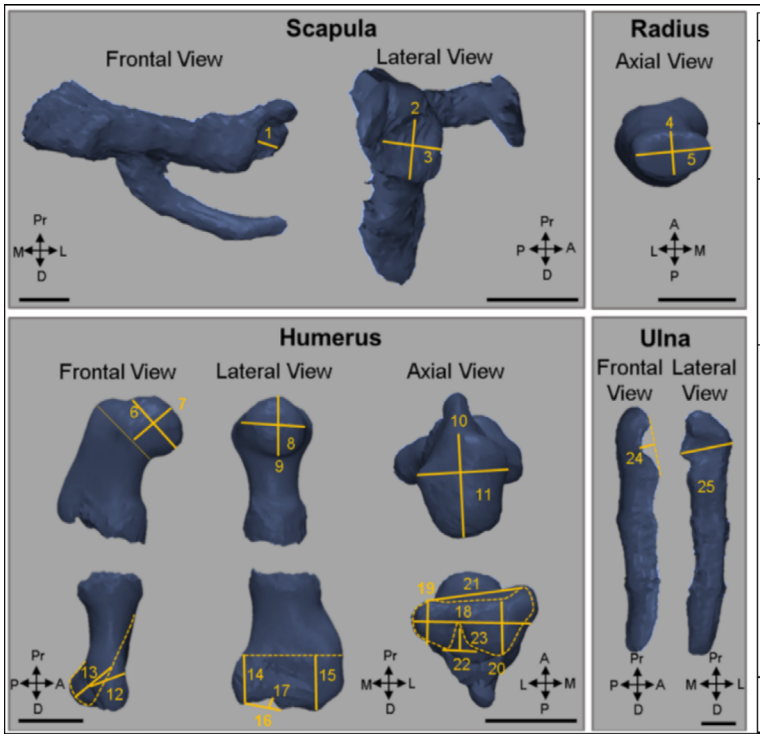

	Measurement
Scapula	1. Glenoid cavity depth
	2. Glenoid cavity height
	3. Glenoid cavity width
Radius	4. Radial head depth
	5. Radial head width
Humeral head	6. Humeral head major axis length
	7. Humeral head minor axis length
	8. Humeral head width
	9. Humeral head height
	10. Humeral head depth
	11. Humeral head axial width
Humeral condyles	12. Lateral condyle width
	13. Medial condyle width
	14. Lateral condyle height
	15. Medial condyle height
	16. Posterior intercondylar width
	17. Posterior intercondylar height
	18. Axial condylar width
	19. Lateral condyle depth
	20. Medial condyle depth
	21. Posterior intercondylar axial width
	22. Anterior intercondylar axial width
	23. Anterior intercondylar depth
Ulna	24. Trochlear notch depth
	25. Trochlear notch width

Fig. 1. Measurements made on forelimb joints. Image adapted from Sotiriou *et al.* (2019). © 2019 Orthopaedic Research Society. Published by Wiley Periodicals, Inc.. Scale bars: 0.5 mm. A, anterior; D, distal; L, lateral; M, medial; P, posterior; Pr, proximal.

dataset. Measurements were performed using Gwyddion image editing software (Gwyddion 2.44; Web ref. 1). As differences in length were previously reported for some muscle-less rudiments (Nowlan *et al.*, 2010), measurements were normalised by the length of the rudiment under investigation, in order to focus the outcomes on shape-specific (rather than overall size dependent) changes.

Rudiment lengths were measured on a lateral view. Mineralisation of the long bones was measured on a frontal cross section of the alizarin red S scans. In cases where the mineralisation extent was uneven between the medial and lateral aspects, the average of the two extents was taken. Mineralisation of the pelvis and scapula was not quantified, due to difficulties in consistent measurement of the mineralisation extent in flat bones. Long bone rudiment lengths, absolute mineralisation extent and mineralisation extent normalised to rudiment length were presented graphically.

All datasets were tested for normality using the Shapiro-Wilk test. For datasets with a normal distribution, two tailed Student's *t*-tests for independent samples (SPSS Statistics 24, IBM corp.) were performed to determine which measurements were statistically significant between control and muscle-less groups. For non-normal datasets, Mann-Whitney tests were performed. Joint shape measurements for which a significant difference ($p < 0.05$) between controls and muscle-less limb mutants were found were displayed graphically, while the full table of results is available on Zenodo (Web ref. 2). To allow for visual assessment of changes in shape, rudiment shape outlines were traced on frontal, lateral and axial sections through the prime regions of interest for each rudiment.

Histology

Cavitation is the physical separation of the rudiments in a synovial joint that facilitates the range and extent

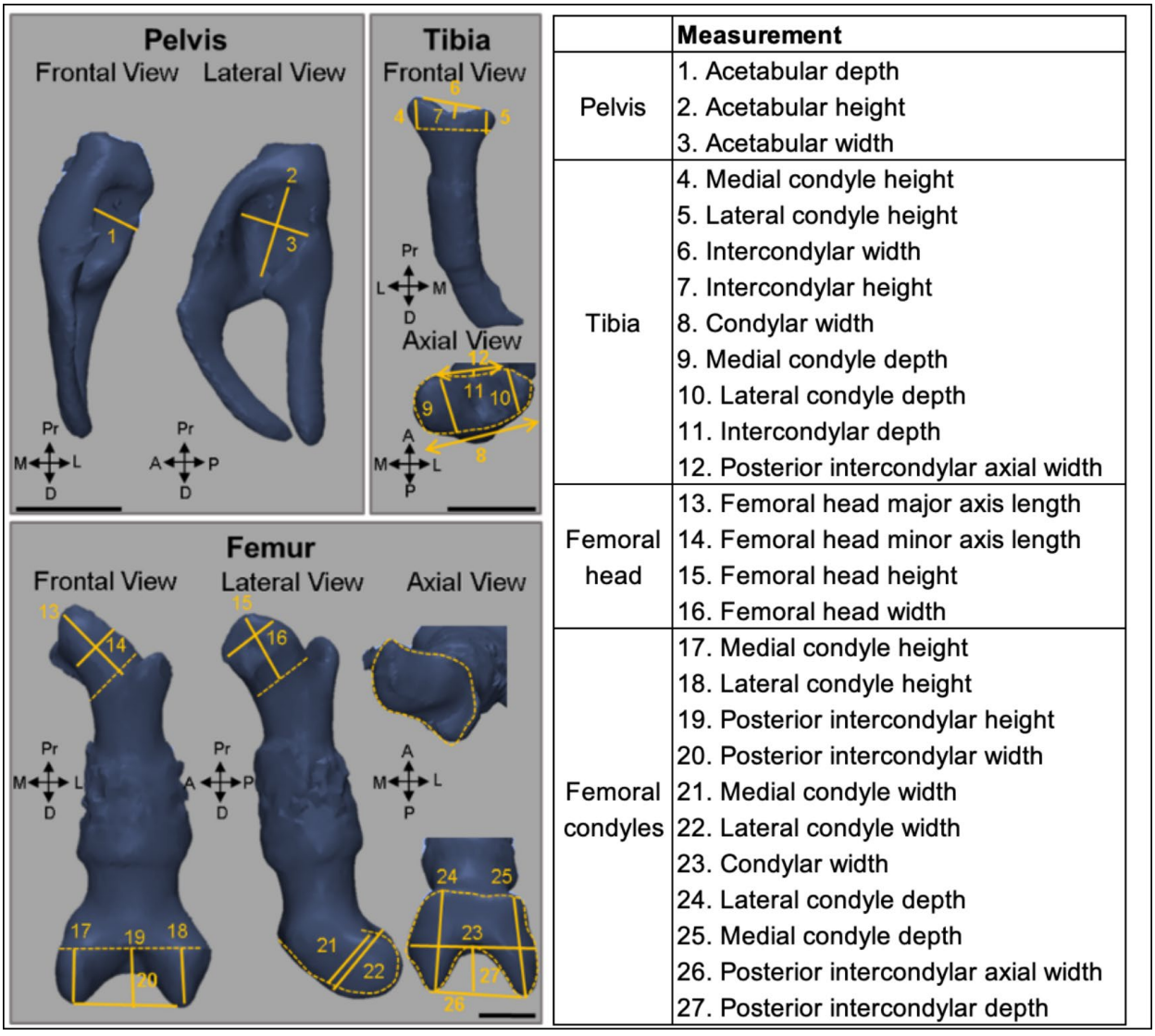

	Measurement
Pelvis	1. Acetabular depth
	2. Acetabular height
	3. Acetabular width
Tibia	4. Medial condyle height
	5. Lateral condyle height
	6. Intercondylar width
	7. Intercondylar height
	8. Condylar width
	9. Medial condyle depth
	10. Lateral condyle depth
	11. Intercondylar depth
	12. Posterior intercondylar axial width
Femoral head	13. Femoral head major axis length
	14. Femoral head minor axis length
	15. Femoral head height
	16. Femoral head width
Femoral condyles	17. Medial condyle height
	18. Lateral condyle height
	19. Posterior intercondylar height
	20. Posterior intercondylar width
	21. Medial condyle width
	22. Lateral condyle width
	23. Condylar width
	24. Lateral condyle depth
	25. Medial condyle depth
	26. Posterior intercondylar axial width
	27. Posterior intercondylar depth

Fig. 2. Measurements made on hindlimb joints. Image adapted from Sotiriou *et al.* (2019). © 2019 Orthopaedic Research Society. Published by Wiley Periodicals, Inc.. Scale bars: 0.5 mm. A, anterior; D, distal; L, lateral; M, medial; P, posterior; Pr, proximal.

of motion of the joint (Pacifici *et al.*, 2005). Cavitation of the glenohumeral (shoulder), elbow, hip and knee joints was assessed in control and muscle-less limb embryos using standard histology. Limbs were dissected and processed for cryo-sectioning in an increasing sucrose gradient (15 % and 30 % sucrose), as described previously (Ahmed and Nowlan, 2020). Processed limbs were embedded in OCT (Agar Scientific, Stansted, UK) diluted with 50 % sucrose and cut (12 μm thickness) using a cryostat (NX70, Leica Biosystems). Then, frozen sections were fixed with 4 % (w/v) PFA, stained with 0.1 % toluidine blue (Sigma-Aldrich) for 3 s and washed with tap water. Following air-drying, sections were imaged by transmitted illumination using a light microscope (Yenway EX30; Life Sciences Microscope, Glasgow, UK).

Chondrocyte morphological properties assessed using high resolution synchrotron phase contrast X-ray tomography

PFA-fixed embryonic limbs were imaged, submerged in ethanol, using synchrotron phase contrast X-ray tomography at the Diamond-Manchester Imaging Branchline I13-2 of the Diamond Light Source synchrotron (Oxfordshire, UK) and the data processed and filtered as described previously (Pierantoni *et al.*, 2021). Each image stack was imported into Materialise Mimics (Leuven, Belgium) and the distal humerus was segmented. Brightness and contrast of the image stacks of all samples were manually corrected using Fiji (Schindelin *et al.*, 2012; Schneider *et al.*, 2012) to the same absolute level to visualise the edges of cells. The 3D spot segmentation plug-in in Fiji (Ollion *et al.*, 2013) was used to identify and label individual chondrocytes throughout the cartilaginous epiphysis.

Firstly, 3D Maxima finder was used to generate a point cloud representing the local maxima in each (putative) cell, referred to as "seeds". The sample images and the seeds were used as inputs for the 3D spot segmentation process. A watershed was applied to define broad areas in which each cell was to be segmented. Next, the extension from local maxima to its corresponding boundary was computed using the Gaussian fit method. Concentric circles centred on the seed were calculated as a radial distribution from the local maxima, which defined the region of interest for intensity calculations around each cell. Then, a Gaussian curve was fitted to the radial distribution and the standard deviation of the curve was used as the threshold value of a cell. Finally, voxels were clustered by means of comparing their intensity to the threshold value. A voxel was considered neighbouring to another within the same cell if its intensity was higher than the local background value, while also being lower than the intensity of the previously clustered voxel, to prevent mixing voxels from cells closed to each other. The output from 3D spot segmentation was an image stack of the same dimension as the original one, with each individual cell assigned a unique label.

3D ellipsoid fitting is another powerful plugin in Fiji (Schindelin *et al.*, 2012) that was used to assign an ellipsoid to each object in an image stack. The output contained measurements of each ellipsoid, including centroid position in an X-Y-Z space, three radii and volume in voxels. To verify the suitability of ellipsoid fitting for quantification of the chondrocyte properties, cell volumes were quantitatively compared between the actual cell volume (as computed by the 3D spot segmentation) to the fitted ellipsoid volume for 500 ellipsoids and no significant differences were found between the actual and fitted volumes. The ellipsoid properties were imported into MATLAB (The MathWorks Inc.) for quantification and visualisation. Overall epiphysis volume was quantified as the volume contained by the cells at the boundaries of the dataset. The volume of a cell (V_c) was the volume of the ellipsoid that was fitted and the cell number was the number of cells identified by the 3D spot segmentation process. ECM volume was computed by subtracting the sum of cell volumes from the epiphysis volume. Cell density was defined as the number of cells per unit volume. A cubic grid system was assigned to each sample in Matlab, with a cube dimension of 80 μm on each side. The 80 μm size was small enough to reflect differential changes within a distal humerus and large enough to accommodate computational demands. Cell density was computed as the number of cells existing in a cube divided by the epiphyseal volume within that cube. Therefore, cell density was correctly adjusted for regions at the edge of the epiphysis. One-way ANOVA with Levene's test for homogeneity of variance was used to test for statistically significant differences between experimental groups ($p < 0.05$). The analyses were performed using SPSS. For each set of ANOVA tests, a *post-hoc* test was carried out. If the data met the assumption of homogeneity of variance, Tukey's HSD *post-hoc* test was used. Otherwise, Games Howell *post-hoc* test was used. Finally, Bonferroni methods were applied to account for multiple comparisons.

Results

TS24 forelimb

Glenohumeral joint

The muscle-less limb glenoid cavity at TS24 was abnormally shaped in the lateral plane when compared to the glenoid cavity of the controls. The outlines of the glenoid cavity of the muscle-less limb scapulae were more elliptical than the controls and exhibited an ectopic protrusion distally (Fig. 3**b**, black arrow). The length-normalised height and width of the glenoid cavity in the muscle-less limb embryos were significantly different from controls (Fig. 4, measurements 2 and 3, respectively). Further shape abnormalities were present in the proximal humerus. The muscle-less limbs had a visibly elongated humeral head in the frontal plane compared to

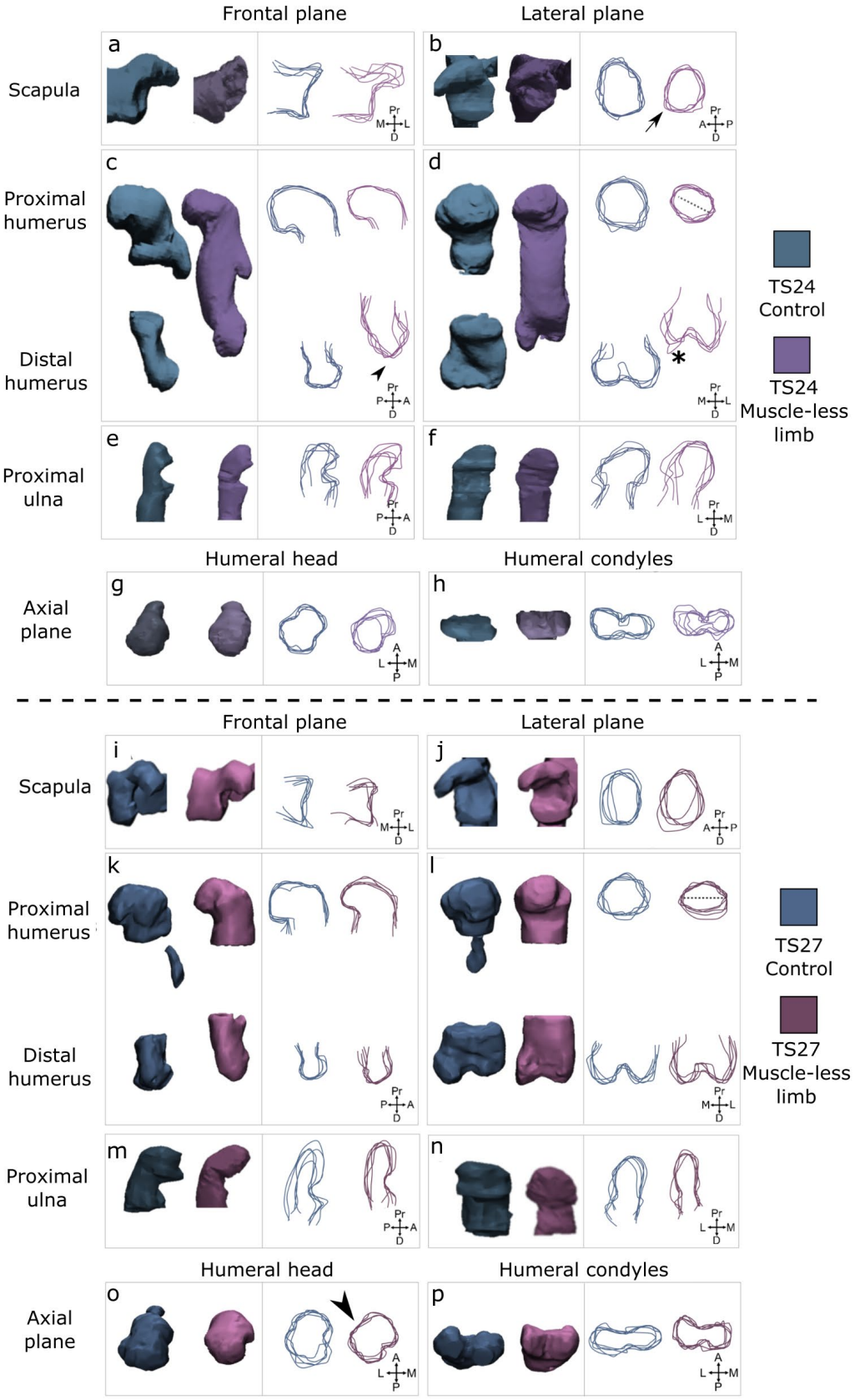

Fig. 3. Qualitative joint shape characterisation of the forelimb joints at TS24 and at TS27. Representative 3D shapes and outlines of the scapula, humerus, radius and ulna of control (blue) and muscle-less limb (purple) embryos. (**b**) Arrow indicates abnormal protrusion of muscle-less limb glenoid cavity. (**c**) Arrowhead represents abnormal shape of distal humerus. (**d**) Asterisk indicates abnormal shape of lateral condyle in distal humerus of muscle-less limbs. (**L**) Dashed line indicates wider appearance of humeral head in the lateral plane. (**o**) Arrowhead indicates the abnormal shape of the muscle-less limb humeral head in the axial plane. A, anterior; D, distal; L, lateral; M, medial; P, posterior; Pr, proximal.

controls (Fig. 3**c**, purple outlines) that was reflected in a significant decrease in the major axis length of the humeral head (Fig. 4, measurement 6). On the lateral plane, the shape of the muscle-less limb humeri was abnormal, resembling an ellipse with a tilted major axis (Fig. 3**d**, dotted line). The glenohumeral joints of the TS24 muscle-less limb embryos were fused, with no clear separation between the glenoid cavity of the scapula and the humeral head (Fig. 5, filled arrowhead).

Elbow joint

The lateral condyle of the TS24 muscle-less limb humerus had an abnormal, angular protrusion on the lateral plane (Fig. 3**d**, asterisk); a result corroborated by the significantly greater posterior intercondylar height (Fig. 4, measurement 17). The lateral condyle of muscle-less limbs was also significantly wider than controls (Fig. 4, measurement 12). The medial condyle of the muscle-less limb humerus was irregular in the frontal plane, with its shape not having the bulbous shape of the controls (Fig. 3**c**, arrowhead). The shape of the muscle-less limb distal humerus in the axial plane varied a lot from sample to sample, whereas that of the controls was more consistent between samples (Fig. 3**h**, outlines). In the rudiments opposing the distal humerus, the ulnae of muscle-less limb were less intricately shaped in the lateral plane than the ulnae of the control embryos (Fig. 3**f**, outlines) and the trochlear notch was significantly wider (Fig. 4, measurement 25). The radii of the muscle-less limb embryos were not different in shape from the controls and no significant differences in the shape of the proximal radii were found. Histologically, the elbow joints were fused at TS24, with no separation between the humeral condyles and the radius and ulna (Fig. 5, filled arrowhead).

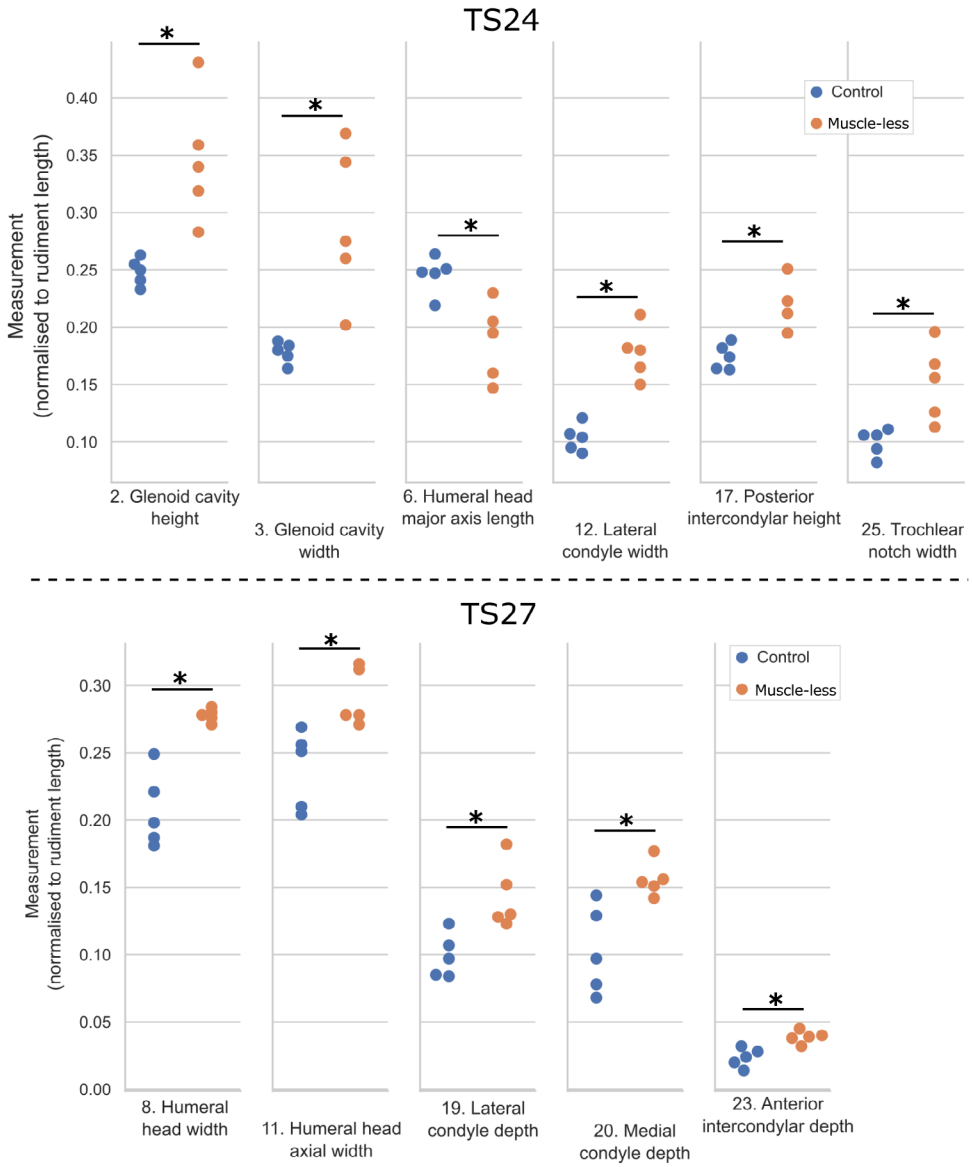

Fig. 4. Quantitative joint shape characterisation of the forelimb joints at TS24 and at TS27. Dot plots illustrating all forelimb measurements with significant differences (* $p < 0.05$) between the muscle-less limb (orange) and control (blue) groups at TS24 and TS27. Numbers shown before each measurement correspond to the measurements illustrated in Fig. 1.

TS27 forelimb

Glenohumeral joint

At TS27, the muscle-less glenohumeral joints were not as pronouncedly different in qualitative shape from the controls as at TS24. No significant differences in the TS27 glenoid cavity were detected. The glenoid cavity was elliptically shaped in both control and muscle-less limb groups and only 1 out of 5 scapulae of the muscle-less limbs still exhibited an abnormal protrusion at the lower end of the long axis (Fig. 3**j**, arrow). The humeral head of the muscle-less limb embryos resembled that of the controls in the frontal plane (Fig. 3**k**) but, in the lateral plane, they were visibly and quantitatively wider compared to the controls (Fig. 3**l**, dotted line and Fig. 4, measurement 8). In the axial plane (Fig. 3**o**), the humeri of muscle-less limbs had an indentation on the antero-lateral aspect (arrowhead) that was not present in the controls and a malformation of the humeral head was also detected through a significant difference in the humeral head axial width (Fig. 4, measurement 10). Therefore, at TS27, the proximal humerus was more severely affected by the lack of muscle than the glenoid cavity. At TS27, cavitation at the glenohumeral joint had consistently occurred in the muscle-less limb embryos (Fig. 5**b**) but with a less prominent separation between the scapula and humeral head that that seen in the controls (Fig. 5, hollow arrowhead).

Elbow joint

The shapes of the distal humerus, proximal radius and ulna at TS27 were qualitatively similar in both control and muscle-less limb embryos in the frontal and lateral planes (Fig. 3**k**-**n**). However, in the axial plane, the muscle-less humeral condyles appeared different from those of controls (Fig. 3**p**), which was reflected in three significantly different measurements all made on the axial plane, namely significantly increased lateral, medial condyle and anterior intercondylar depths in the muscle-less limbs compared to the controls (Fig. 4, measurements 19, 20 and 23, respectively). There were no significant differences in the proximal ulna between the muscle-less limb and control groups at TS27. As at TS24, no shape or size differences were observed between the radii of the two groups at TS27. The elbow joint continued to be fused at TS27 (Fig. 5, filled arrowhead). Therefore, a partial recovery of elbow joint shape occurred in the forelimb joints of muscle-less limb by TS27, despite the lack of cavitation.

TS24 hindlimb

Hip joint

At TS24, the acetabulum was qualitatively and quantitatively deeper and wider in the muscle-less limb group than in the controls (Fig. 6**a**, Fig. 7; measurements 1 and 3). The shape of the acetabulum in muscle-less limbs was also more variable in the lateral plane than in controls (Fig. 6**b**). The femoral head of muscle-less limbs appeared longer and more slender (Fig. 6**c**,**d**) and significantly higher (Fig. 7, measurement 15) than in controls. These features in the proximal femur of muscle-less limbs may indicate an adjustment of femoral head shape to the deeper concavity of the acetabulum. At TS24, the hip joint of control limbs was clearly separated (Fig. 8), while the hip of muscle-less limbs was fused, with no separation between the femoral head and the acetabulum (Fig. 8, arrowhead).

Knee joint

On the frontal plane, both muscle-less limb femoral condyles at TS24 had a more angular shape when compared to the condyles of the controls, with the intercondylar region resembling a triangle rather than a curve (Fig. 6**c**), as reflected in a significant difference in the posterior intercondylar width (Fig. 7, measurement 20). The lateral condyle of the muscle-less limb tibiae protruded more prominently out from the diaphysis than controls (Fig. 6**e**, arrowhead), as reflected in a significant increase in the tibial

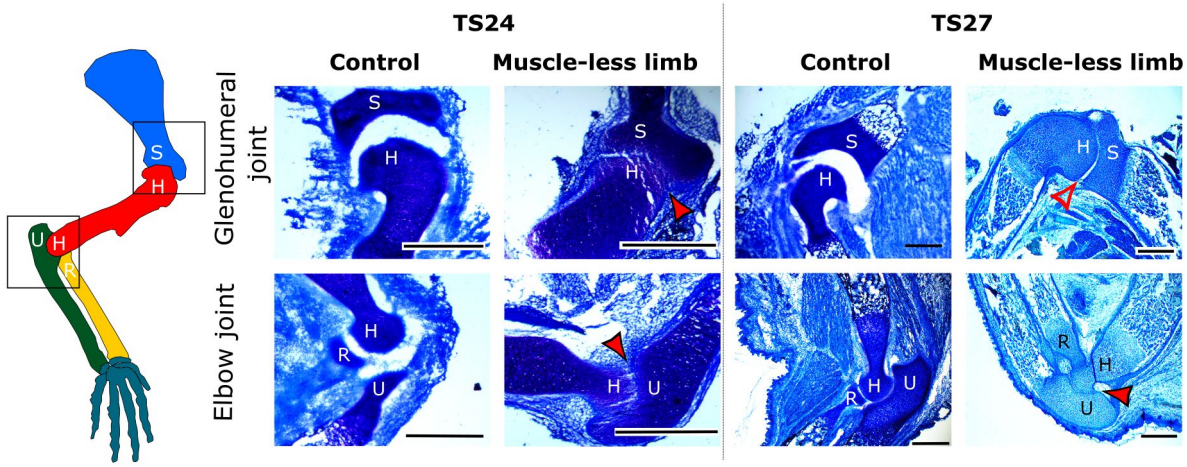

Fig. 5. Cavitation in the forelimb joints at TS24 and TS27. S: scapula; H: humerus; U: ulna; R: radius. The glenohumeral joints at TS24 were not cavitated (filled arrowheads), with partial cavitation at TS27 (hollow arrowhead). The elbow joints were fused at both TS24 and TS27 (filled arrowheads). Representative images shown. The results were consistent for all 3 samples per stage. Scale bars: 500 μm.

lateral condyle height in the muscle-less limb group compared to controls (Fig. 7, measurement 5). Knee joints of the muscle-less limb embryos were fully cavitated at TS24, as was the knee joint of the control embryos at the same stage (Fig. 8).

TS27 hindlimb

Remarkably, the shape of both the hip and the knee joints of the muscle-less-limb embryos at TS27 resembled in shape those of the controls (Fig. 6). None of the obvious shape differences seen at TS24 remained. This was corroborated by the lack of significant differences in any of the measurements performed on the articular surfaces, comprising the two joints at TS27. The hip joint of the TS27 muscle-less limb embryos remained fused, as no separation was seen between the femur and the acetabulum (Fig. 8, arrowhead), while the muscle-less limb knee joint remained fully cavitated (Fig. 8). Therefore, in muscle-less limb-embryos at TS27, both hip and knee joint shape recovered until being equivalent to control shapes, despite the continued lack of cavitation in the hip joint.

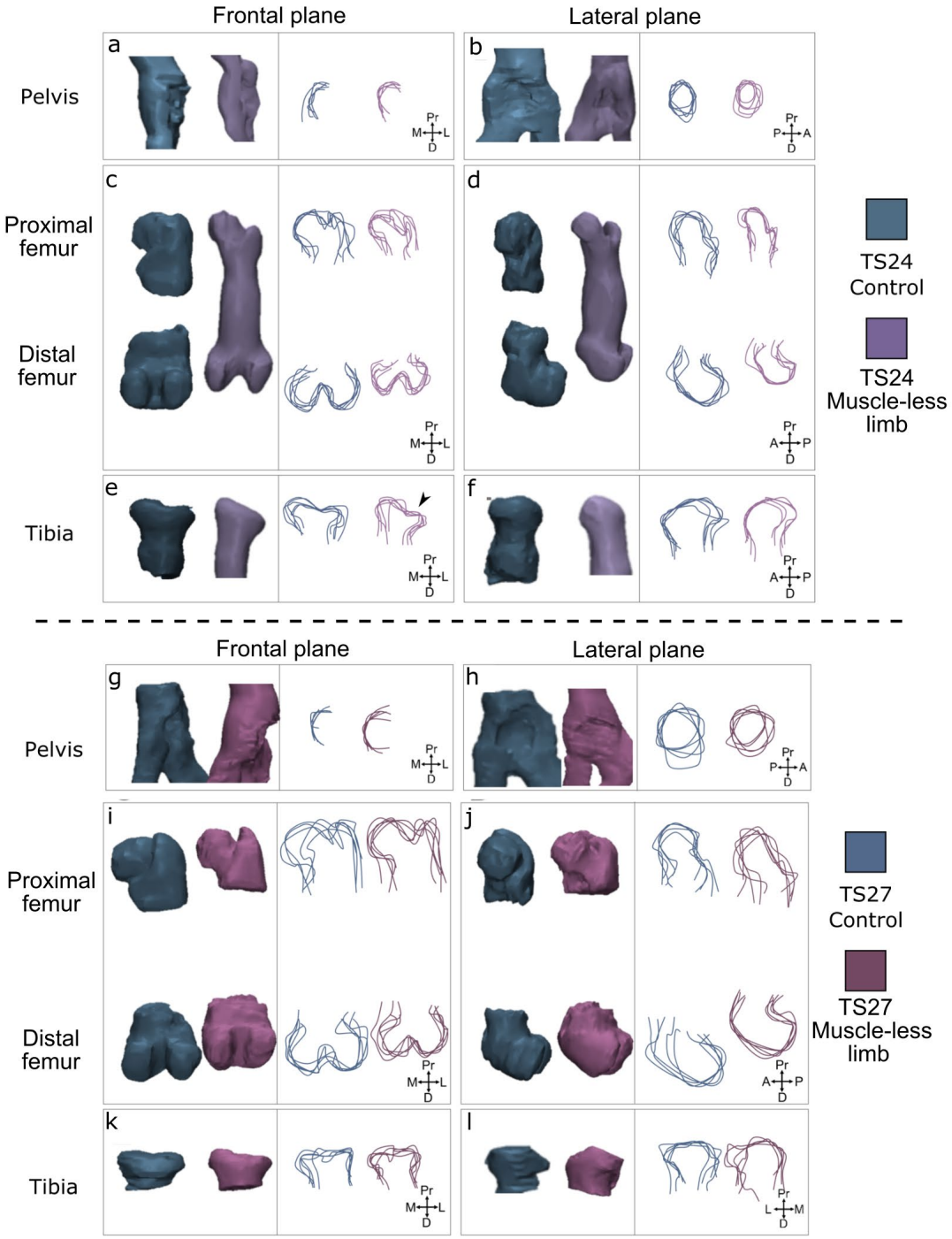

Fig. 6. Qualitative joint shape characterisation of the hindlimb joints at TS24 and at TS27. Representative 3D shapes and outlines of the pelvis, femur and tibia of control (dark blue) and muscle-less limb (dark purple) embryos. (**e**) Arrowhead indicates abnormal shape of the proximal tibia. A, anterior; D, distal; L, lateral; M, medial; P, posterior; Pr, proximal.

Chondrocyte morphological properties

At least 33,000 cells per sample were morphologically assessed, as detailed in Table 1. Morphological abnormalities, and in particular the abnormal protrusion of the medial condyle, were evident in the muscle-less limbs at both TS24 and TS27 (Fig. 9**a**). Calculations of epiphyseal volume showed no significant differences in epiphyseal volume between muscle-less limbs and controls at TS24 and significantly reduced volume in the muscle-less limbs compared to the control limbs at TS27 (Fig. 9**b**). While this result appears somewhat contradictory to the results of the shape feature measurements, the latter were normalised to rudiment length (which is known to be decreased when skeletal muscle is absent), while the phase contrast data were not normalised to rudiment length, as the entire rudiment was not imaged. Cell numbers were the same between TS24 and TS27, while there was a significant decrease in cell number in the TS27 muscle-less limbs compared to stage-matched controls (Fig. 9**c**), correlating with trends observed for overall epiphysis volume (Fig. 9**b**). However, matrix proportion (Fig. 9**d**) and cell density (Fig. 9**e**) were similar between control and muscle-less limb groups at both stages and the decrease in epiphyseal volume at TS27 was likely linked to the absolute reduction in cell number at that stage. The most pertinent temporal changes between muscle-less limb and controls at the cell morphology level were in cell volume. Cell volume dramatically increased between TS24 and TS27 in both muscle-less and control groups, as shown in Fig. 9**f**. However, relevant to the partial recovery of shape in the muscle-less limbs at the later stage, cell volume in the muscle-less limbs was significantly ($p < 0.05$) smaller than in controls at TS24 but had recovered by TS27 (Fig. 9**f**). The average (± standard deviation) cell volume at TS24 was 47.6 ± 5.8 μm^3 in the controls and 33.5 ± 8.7 μm^3 in the muscle-less limbs, and at TS27, 93.1 ± 17.9 μm^3 in the controls and 102.1 ± 14.0 μm^3

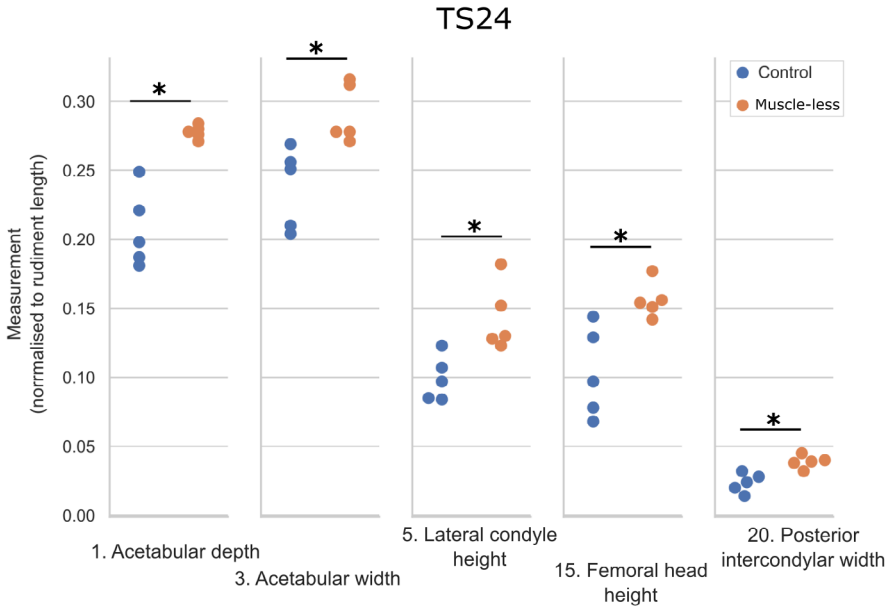

Fig. 7. Quantitative joint shape characterisation of the hindlimb joints at TS24. Dot plots illustrating all hindlimb measurements with significant differences (* $p < 0.05$) between muscle-less limb (orange) and control (blue) groups at TS24. No measurements of the hindlimb joint shapes showed any significant differences at TS27. Numbers shown before each measurement correspond to the measurements illustrated in Fig. 2.

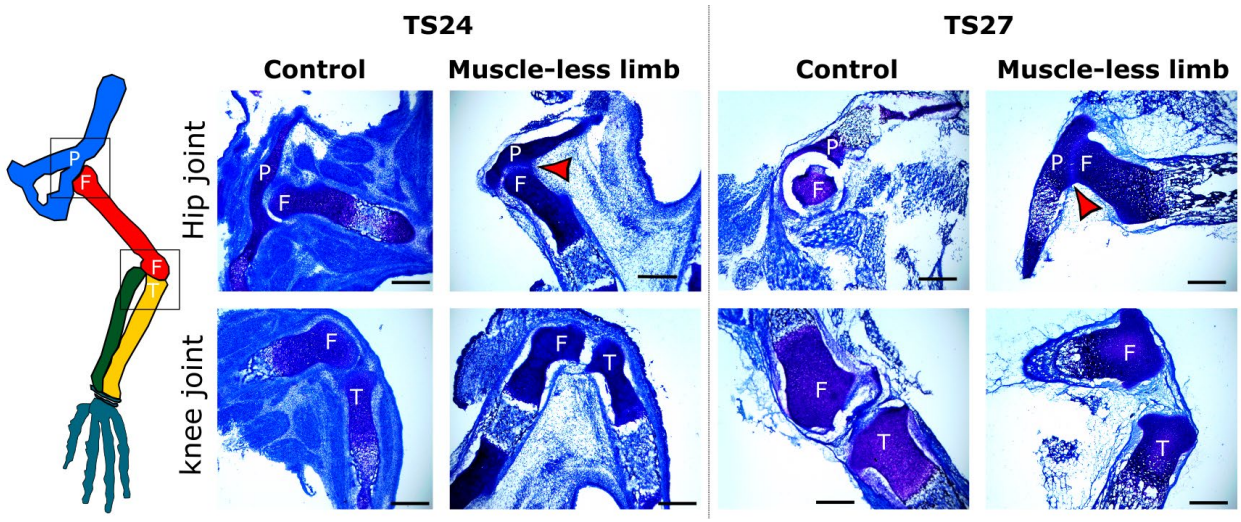

Fig. 8. Cavitation in the major hindlimb joints at TS24 and TS27. P: pelvis; F: femur; T: tibia. Cavitation was absent in the hip joint at TS24 and TS27 and present in the knee joint at both stages. Representative images shown. The results were consistent for all 3 samples per group/stage. Scale bars: 500 μm.

Table 1. Number of cells quantified for each sample.

Limb	1	2	3	4
TS24 control	64,586	69,552	94,701	67,207
TS24 muscle-less limb	32,905	82,769	123,469	71,995
TS27 control	170,413	197,570	233,387	245,190
TS27 muscle-less limb	161,111	163,876	86,338	75,093

in the muscle-less limbs. In conclusion, a recovery in cell volume in the muscle-less limbs by TS27 is likely to have contributed to the partial recovery in shape at the same stage.

Rudiment length and mineralisation

Forelimb

At TS24, the humerus, ulna and radius were all significantly shorter than controls at the same stage (Fig. 10). At TS24, these three rudiments also had significantly reduced mineralisation in muscle-less limbs compared to controls, for both absolute mineralisation extent and adjusted for rudiment length (Fig. 10). At TS27, the humeri and ulnae of muscle-less limbs were still significantly shorter than controls, while there was no significant difference between the muscle-less and control radii (Fig. 10). A dramatic change in mineralisation progress occurred by TS27. Mineralisation of the three forelimb rudiments of muscle-less limbs "caught up" with controls of the same age, with no significant reductions in absolute or length-proportionate mineralisation in any of the three rudiments. In fact, the proportion of mineralisation in the ulnae of muscle-less limbs at TS27 significantly exceeded that of the controls (Fig. 10).

Hindlimb

At TS24, both the femur and tibia were significantly shorter in the muscle-less limbs than in the controls and the mineralisation extent of these rudiments (absolute and length normalised) was also significantly reduced in the muscle-less limbs compared to the controls (Fig. 11). By TS27, there was no longer a significant difference in femoral length between the groups, while the tibia was still significantly shorter in the muscle-less limbs than in the controls (Fig. 11). As in the TS27 forelimb, mineralisation of the rudiments muscle-less hindlimbs had recovered with respect to controls of the same age, with no significant reductions in absolute or length-proportionate mineralisation relative to controls (Fig. 10). As with the ulna, mineralisation of the tibia (adjusted for rudiment length) exceeded that of the control (Fig. 11).

Discussion

By the latest prenatal stage (TS27/e18.5), joint shape, rudiment length and rudiment mineralisation were less severely affected by the absence of skeletal muscle than earlier in development (TS24/e15.5). Recovery of joint shape in the muscle-less limbs at TS27 was more pronounced in the hindlimb than in the forelimb, with the hip and knee joint exhibiting no significant differences in measurements between the muscle-less limbs and controls at TS27. Cell volume was significantly reduced in the muscle-less limb distal humerus at TS24, compared to the control limbs at the same stage. However, by TS27, there was no significant differences in cell volume between muscle-less limb and controls, suggesting that a recovery in cell volume is contributing, at least in part, to the recovery of joint morphology in the muscle-less limb late in gestation. The lengths of the femur and radius of muscle-less limbs recovered to those of the controls by TS27, while all other rudiments of muscle-less limb were still shorter than controls at TS27. The recovery in mineralisation in the muscle-less limbs over gestation was dramatic, with mineralisation of the TS27 muscle-less limb long bone rudiments catching up with mineralisation in controls. Only cavitation provided limited evidence for recovery with advancing gestation in the muscle-less limbs. Joints that had not cavitated at TS24 remained completely or almost completely not cavitated at TS27. Only the glenohumeral joint showed an improvement in cavitation status with advancing developmental age.

Although active muscle contractions are completely absent in the limbs of the Splotch-delayed mouse embryos, there are still two sources of mechanical stimulation acting on or in the rudiments. The first is mechanical stimulation from passive movements due to the activity of the mother and the wild-type littermates. Computational models have been previously used to predict the stresses and strains induced in the developing rudiments by i) skeletal muscle contractions and ii) a very small (10 μm) deflection of the limb such as would occur due to passive movements (Nowlan *et al.*, 2012). The models predicted that the stresses induced by skeletal muscle contractions are much lower than those induced by limb movements, indicating that it is the movements of the limb that result from skeletal muscle contraction that provide the dominant mechanical stimulation of the tissues and structures (Nowlan *et al.*, 2012). While passive movements may have a negligible effect in wild-type embryos (due to the far larger active movements induced by muscle contractions), it is reasonable to believe that passive movements could play a role in the recovery of aspects of skeletal development in the muscle-less limb mice. As pregnancy progresses, the space each embryo has decreases, which could increase the intensity and impact of passive stimuli on the muscle-less limbs,

potentially contributing to the recovery of joint shape, rudiment growth and rudiment mineralisation. The other source of mechanical stimulation acting during development, including in the muscle-less limbs, is growth-generated strains and pressures. First proposed as acting as a complex field of morphogens influencing early limb morphogenesis in 2002 by Henderson and Carter, growth-generated strains and pressures arise during development when "complex configurations of connected tissues grow at different rates", leading to "the generation of time-varying, quasi-static stresses and strains throughout the developing cells and tissues" (Henderson and Carter, 2002). During prenatal development with normal skeletal muscle and movements, growth-related strains and pressures may play a minor role once movements have commenced. However, when skeletal muscle is absent, the biophysical stimuli arising from growth-related strains and pressures could contribute to growth, morphogenesis and differentiation in the skeleton.

The advance provided by the present work is that it is the first demonstration of partial or full recovery of joint shape, rudiment length and rudiment mineralisation from the effects of absent skeletal muscle by the latest prenatal stage. Intriguingly, cavitation (the physical separation of the rudiments that facilitates the full range of motion of the joint) was the only aspect not to recover to some extent over development. This may indicate that cavitation is a single "rupture" type event, as previously proposed (Drachman and Sokoloff, 1966), and if movement

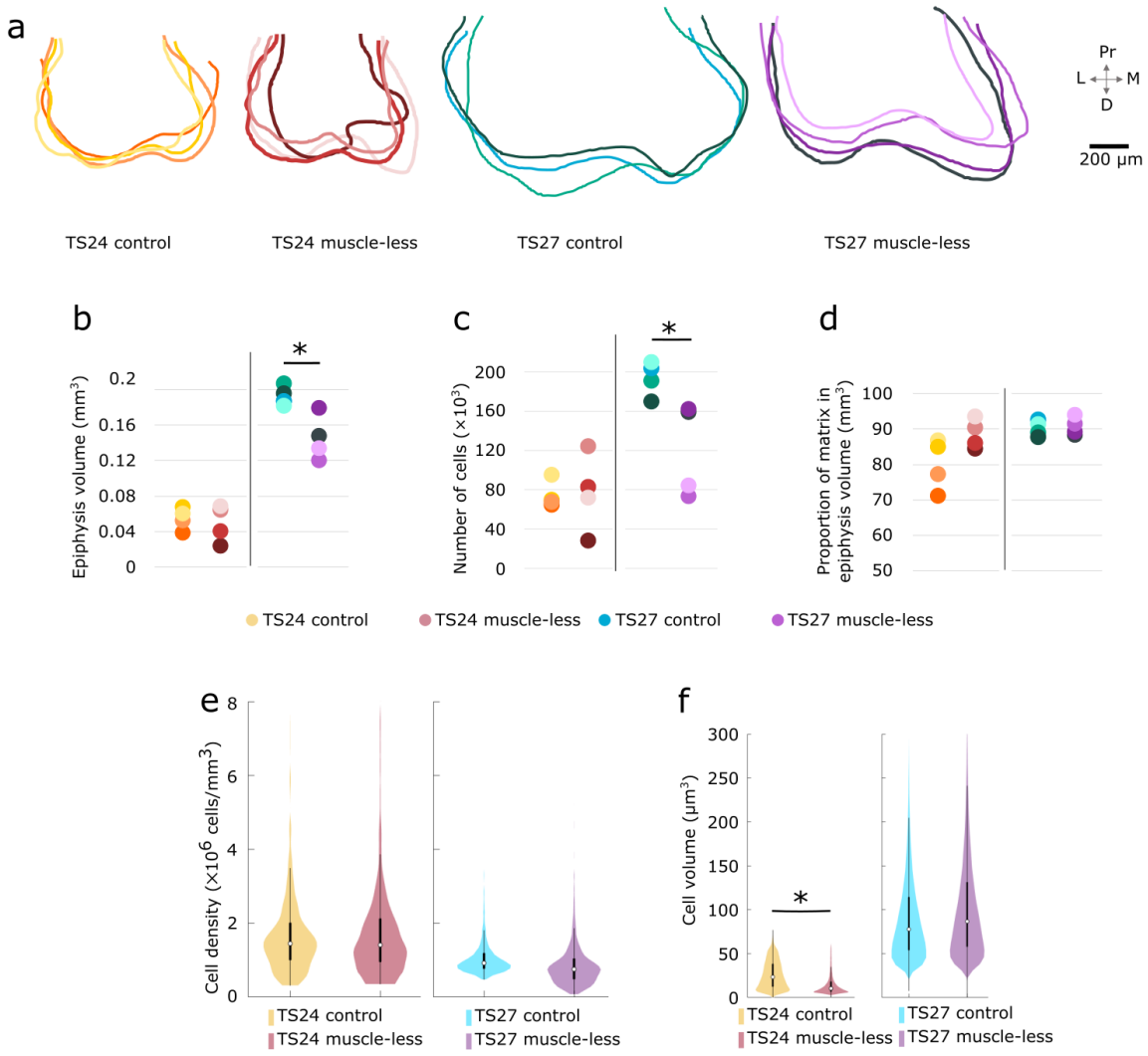

Fig. 9. Imaging using synchrotron phase contrast X-ray tomography of muscle-less limb and control distal humeri revealed cell level morphological abnormalities in the muscle-less limbs. (**a**) Outlines of shape from mid-sagittal plane of each limb imaged in 3D illustrating the shape abnormalities in the muscle-less limb mice. Scale bar: 200 µm. (**b**) Epiphyseal volume and (**c**) number of cells were similar between control and muscle-less limbs at TS24, while at TS27, the muscle-less limbs had a significantly reduced volume and cell numbers compared to controls. (**d**) Matrix proportions and (**e**) cell density in the distal humerus were similar between control and muscle-less limb embryos at both stages examined. (**f**) Cell volume was significantly lower in the muscle-less limb mice than in controls at TS24, with no remaining significant differences in cell volume between groups by TS27. * $p < 0.05$ between muscle-less limb and controls within each age category. D, distal; L, lateral; M, medial; Pr, proximal.

does not occur at the critical time, the opportunity for normal cavitation is lost. It is feasible that active bending movements, localised to the joint, are needed for cavitation to occur, which would not occur even with increasing growth-generated stresses or strains due to passive movements. This concurs with a recent study in which a cavity was artificially induced in the developing chick using an applied bending movement (Bridglal *et al.*, 2021). What was surprising in the present study was the partial or complete recovery in joint shape despite the lack of, or incomplete, cavitation in the glenohumeral, elbow and hip joints, which contradicted a prior understanding of joint shape being heavily dependent on successful cavitation (Bridglal *et al.*, 2021). Another interesting feature of the joint shape results was that, in the glenohumeral and elbow joints, different features were more abnormal at TS27 than at TS24. This could imply that, as the joints continue to grow, the opposing surfaces are continually shaping and moulding each other, providing the opportunity for some internal correction of early abnormalities. Shape abnormalities newly arising at TS27 could be due to some form of compensation for early shape abnormalities in the opposing surface or, alternatively, particularly in the elbow joint, to the continued joint fusion. However, as the hip joint did not have any quantitative shape differences at TS27, despite the ongoing lack of cavitation, this would indicate that perhaps local interaction between

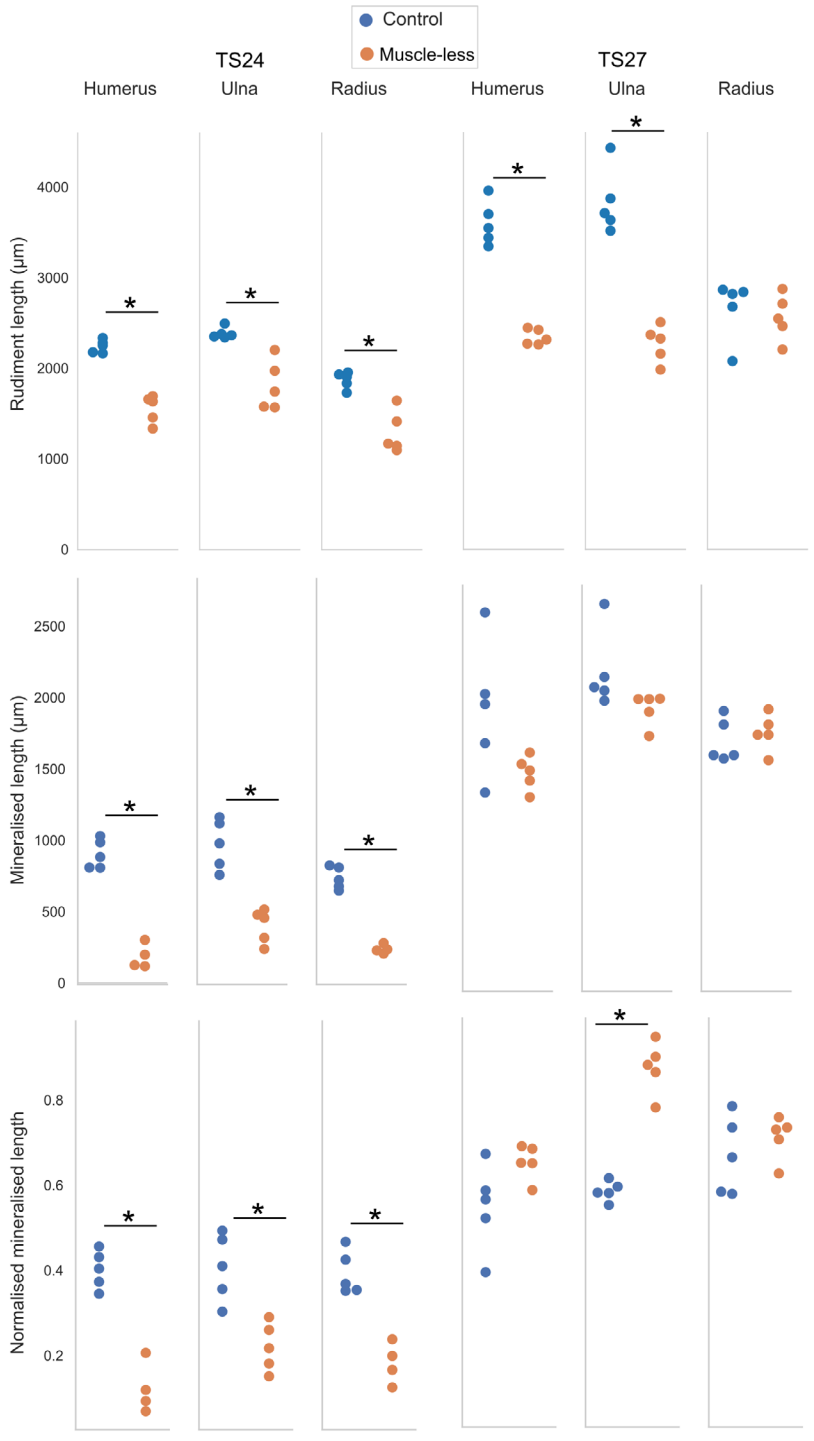

Fig. 10. Forelimb rudiment length and mineralisation. At TS24, all length and mineralisation measurements were significantly reduced in muscle-less forelimbs (orange) compared to controls (blue). At TS27, humeri and ulnae were still significantly smaller in the muscle-less limbs, while all mineralisation extent measures had recovered, or even exceeded, those of littermate controls. Normalised mineralisation lengths calculated by mineralised length divided by rudiment length (equivalent to mineralised proportion). * $p < 0.05$.

opposing joint surfaces is the primary driver of shape recovery, rather than the capacity for movement at the joint.

One of the most fascinating findings was the remarkable recovery of mineralisation extent in the muscle-less limbs between TS24 and TS27, with two rudiments (the ulna and tibia) at TS27 having significantly more mineralisation (proportionate to rudiment length) compared to controls at the same stage. What prompted the dramatic acceleration in mineralisation over the 3 d period between TS24 and TS27? Progression of the growth plates and of mineralisation has been shown to be promoted by cyclic hydrostatic pressure (Henstock *et al.*, 2013) or applied compression loading (Khatib *et al.*, 2021). It is possible that as the embryo grows and becomes more restricted when approaching birth, the increasing levels of biophysical stimuli induced in the skeletal rudiments could accelerate mineralisation sufficiently so that the initial delay in bone formation is recovered. Additional insights can be garnered from analyses of growth plate and mineral structure in humeri of muscle-less and control limbs, as previously described (Pierantoni *et al.*, 2021). Bone volume and total volume were significantly lower in humeri of muscle-less limbs than in controls at TS24, but there were no significant differences between the groups at TS27, corroborating the findings of the present study on humeral mineralisation extent. Bone volume fraction in the humerus was similar between muscle-less limb and control humeri at all stages studied, indicating that the lack of muscle may affect the rate of mineralisation, rather than the actual mineral being deposited. At the level of the growth plate, there were no differences in the relative proportions of the hypertrophic and proliferating zones of the growth plate between the muscle-less limb and control groups at any stage, indicating that a lack of muscle did not strongly influence the overall morphology of the growth plate. Chondrocyte volumes appeared smaller in the growth plates of muscle-less limbs than in the controls at both TS24 and TS27, which could be a contributing factor to the sustained lower length of the humerus by TS27. Chondrocyte density appeared lower in the hypertrophic and proliferating zones of the growth plate of muscle-less limbs at TS24 compared to the controls but equivalent chondrocyte density in both regions was recovered in the muscle-

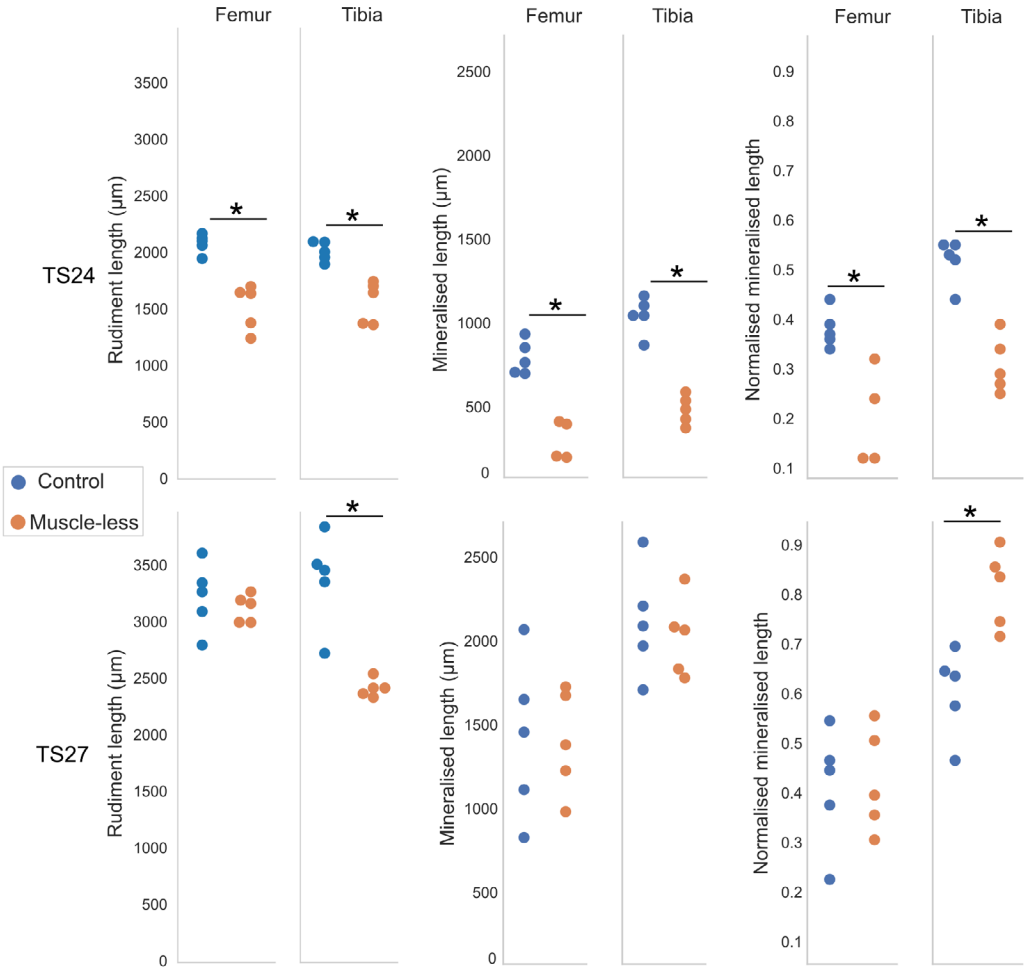

Fig. 11. Hindlimb rudiment length and mineralisation. At TS24, femoral and tibial length and mineralisation measures were significantly reduced in muscle-less limbs (orange) compared to controls (blue). At TS27, tibial lengths were still significantly lower in the muscle-less limbs, while mineralisation extent measures had recovered, or even exceeded, those of littermate controls. Normalised mineralisation lengths calculated by mineralised length divided by rudiment length (equivalent to mineralised proportion). * $p < 0.05$.

less limbs by TS27 (Pierantoni *et al.*, 2021). Therefore, chondrocyte proliferation could be a candidate marker for monitoring late-gestation recovery of mineralisation in the muscle-less limb mice.

The question remains as to why mineralisation in the muscle-less limbs recovered to the extent of controls in all rudiments by TS27, when rudiment length only recovered in the radius and femur. The data raised the possibility that both rudiment length and mineralisation are mechanoregulated in different ways. The growth of the prenatal rudiment, prior to initiation of the primary ossification centre, occurs due to proliferation and expansion of the transient cartilage. After initiation of diaphyseal ossification, the transient cartilage still contributes to overall growth, as evidenced by the data presented in the present study on expansion of epiphyseal chondrocyte volume between TS24 and TS27. The transient chondrocytes and the growth plate chondrocytes in the embryonic limb may be differentially regulated by mechanical loading, with the growth plate chondrocytes responding at a lower threshold of loads. Alternatively, or perhaps additionally, an increase in biophysical stimuli with advancing gestational age may not be able to consistently rescue rudiment length due to the rapidly decreasing quantities of transient cartilage remaining in the rudiment as development progresses. It is worth highlighting that the recovery in mineralisation extent does not necessarily mean a recovery in the ossification process, as the mineral deposited in the muscle-less limbs could be abnormal or inferior in quality. Indeed, a recent study has reported abnormal structure and localisation of key collagens in the cartilage of muscle-less limbs and mineralised cartilage at and prior to TS27 (Ahmed *et al.*, 2022), indicating indeed that the tissue does not recover by the latest prenatal stage. A useful future avenue of research would be to assess the mechanical properties of cartilage and mineralised cartilage of muscle-less limbs, providing insight into the quality and function of the tissues of the developing limb when skeletal muscle is absent.

Surprisingly, the proportions of ulna and tibia mineralisation were significantly larger in the muscle-less limbs than in controls at TS27. In muscle-less limbs, ulnae and tibiae remained significantly shorter than in controls at TS27 and, therefore, a recovery in mineralisation (back to the extent of mineralisation in control ulnae and tibiae) led to the larger mineralisation proportion in the muscle-less limbs. Both the ulna and tibia are the dominant rudiments in the zeugopod (the middle section of the limb). They would likely be subjected to lower biophysical stimuli from passive movements compared to the stylopod (most proximal region of the limb), due to greater bending moments in the stylopod. This could be a contributing factor to slower growth (and reduced length) in the zeugopod rudiments of muscle-less limbs. Another possibility is that the accelerated mineralisation of the zeugopod is due to an increased level of growth-generated strains based on the restraint between the strong stylopod rudiment and the complex set of joints at the paws, with lateral restraint due to the presence of the radius or fibula.

The present study adds a novel insight into the cell-level mechanisms underlying prenatal joint growth and morphogenesis. While the increase in cell volume is a well-described phenomenon underlying the expansion of the rudiment at the growth plate (when chondrocytes undergo hypertrophy) (Hunziker, 1994), the study data were the first to describe a dramatic increase in cell volume, late in gestation, in the (transient) epiphyseal cartilage of the prenatal long-bone rudiment. Trends in cell number were correlated with changes in overall volume across the two groups and two timepoints but not with the recovery of shape at TS27. Average cell volumes in the muscle-less limbs were approximately 30 % smaller than those in the control littermates at TS24, while cell volumes were similar between the two groups by TS27. As there were no differences between muscle-less limb and control groups in cell density, or in the proportion of matrix volume, at either of the stages examined, cell volume is the most likely cell-level mechanism underlying the partial or full recovery of joint shape by the latest prenatal stage. Future work is planned to rigorously test this hypothesis.

There are some limitations to the study. The first is that the number of animal used was quite small, with a group size of 5. However, the results were reasonably consistent, with variation within groups dwarfed by the variation between control and muscle-less limb groups, as can be seen from both the raw data (dot plots) and the rudiment outlines. Sample numbers were unfortunately insufficiently powered to test the hypothesis that the proximity or number of normally moving littermates influenced skeletal development of the muscle-less limb embryos. As murine embryos are sequentially arranged in the uterus, the limbs of the embryos interact with the uterine wall rather than with other embryos and, therefore, it is the authors belief that the dam's movements would have dominated the induction of passive movements. Another limitation was that the method of normalising shape measurements to rudiment length had the potential to disproportionately skew shape features that may not change in proportion to length. However, it was reassuring that significantly different measurements correlated with shape abnormalities visible in the outlines and that shape recovery at TS27 was evident both in the qualitative and the quantitative analyses. As *Pax3* mutation is neonatal lethal, it was unfortunately not possible to quantify the effects of absent skeletal muscle on a longer timescale than the one used in the present study. Despite the dramatic improvement in the various parameters of skeletal development studied by TS27, the skeletons would not be expected to be normally functioning after birth (if, in theory,

the mice would survive). The lack of cavitation, in particular, would inhibit movement and potentially lead to new or worsening joint shape abnormalities. Furthermore, even very slight shape abnormalities not detected by the performed measurements would likely impact on function and health of the joint. For example, the shape abnormalities involved in hip dysplasia are not always very dramatic and yet, with growth and over time, there are severe consequences for gait and joint health.

The relevance of the present study for human conditions is that multiple aspects of the developing murine skeleton have the capacity for recovery despite the absence of skeletal muscle and the active movements resulting from muscle contractions. Developmental dysplasia of the hip and amyoplasia result from a period of abnormal or restricted intra-uterine movement (Nowlan, 2015). Hip dysplasia is diagnosed using ultrasound from 4 postnatal weeks (Tan *et al.*, 2019) and amyoplasia (despite its quite dramatic impact on skeletal morphology) is diagnosed prenatally in only 22.2 % of cases (Filges and Hall, 2013). Could it be the case that the incidence of skeletal abnormalities is much greater *in utero* but that most of these have self-corrected and resolved prior to birth? Many cases of hip instability in neonates resolve without any intervention (Bialik *et al.*, 1999) and hip dysplasia is likely more a spectrum than a dichotomous diagnosis, where potentially only the most severe cases do not spontaneously recover either prenatally or postnatally. The fact that restricted movement postnatally, for example in a cradle board (Dezateux and Rosendahl, 1997), can induce hip dysplasia in formerly healthy hips further demonstrates the critical role of muscle, movements and mechanics in healthy skeletal development. Given that both late or missed diagnoses of hip dysplasia are a significant issue, usually necessitating surgery (Broadhurst *et al.*, 2019), it is also possible that a hip joint that satisfies the screening criteria in early postnatal life could adapt and adjust its shape negatively as the baby grows. A key question which was not answerable by the present study is how the ability to self-correct and recover abnormal skeletal development declines over postnatal development. If the adaptation potential of the developing skeleton declines over postnatal development, it may make sense to harness the plasticity of the developing skeleton at as young an age as possible through physical therapy, casting or harnesses. This question will be explored in future work, with an alternative postnatal animal model.

In conclusion, skeletal development was studied at two different prenatal ages in the muscle-less limb mouse. With advancing prenatal development, the effects of absent muscle on all parameters, apart from joint cavitation, become less severe. Joint shape, rudiment length and rudiment mineralisation were significantly abnormal in multiple rudiments at TS24 but such abnormalities partially or completely recovered in all rudiments by the prenatal stage TS27. Cell-level data analyses revealed that a recovery in cell volume in the muscle-less limbs over the developmental timescale examined is a likely contributor to recovery at the joint level. In contrast, joint cavitation did not recover from the lack of skeletal muscle over development. Understanding how mammalian bones and joints continue to develop in an environment without muscle contractions, but with mechanical stimulation due to the movement of the mother, provides important insights into conditions affecting human babies, such as developmental dysplasia of the hip and arthrogryposis. The present study animal model data would suggest that the effects of immobility *in utero* may reduce in severity as development progresses.

Acknowledgments

This work was funded by the European Research Council under the European Union's Seventh Framework Programme (ERC Grant agreement number 336306) and by a Royal Society International Exchange Grant. We thank Diamond Light Source for providing beamtime at the Diamond-Manchester Imaging Branchline I13-2 (proposal MT16557) and Andrew Bodey, Sophie Le Cann, Elin Törnquist and Aurélie Levillain for their assistance.

References

Ahmed S, Nowlan N (2020) Initiation and emerging complexity of the collagen network during prenatal skeletal development. Eur Cell Mater **39**: 136-155.

Ahmed S, Rogers AV, Nowlan NC (2022) Mechanical loading due to muscle movement regulates establishment of the collagen network in the developing murine skeleton. Dev Biol. DOI: 10.1101/2022.06.23.497302.

Bialik V, Bialik GM, Blazer S, Sujov P, Wiener F, Berant M (1999) Developmental dysplasia of the hip: a new approach to incidence. Pediatrics **103**: 93-99.

Bridglal DL, Boyle CJ, Rolfe RA, Nowlan NC (2021) Quantifying the tolerance of chick hip joint development to temporary paralysis and the potential for recovery. Dev Dyn **250**: 450-464.

Broadhurst C, Rhodes AML, Harper P, Perry DC, Clarke NMP, Aarvold A (2019) What is the incidence of late detection of developmental dysplasia of the hip in England? A 26-year national study of children diagnosed after the age of one. Bone Joint J **101-B**: 281-287.

Brunt LH, Skinner REH, Roddy KA, Araujo NM, Rayfield EJ, Hammond CL (2016) Differential effects of altered patterns of movement and strain

on joint cell behaviour and skeletal morphogenesis. Osteoarthritis Cartilage **24**: 1940-1950.

Dezateux C, Rosendahl K (1997) Developmental dysplasia of the hip. Lancet **369**: 1541-1552.

Drachman DB, Sokoloff L (1966) The role of movement in embryonic joint development. Developmental Biology **14**: 401-420.

Drachman DanielB, Coulombre AlfredJ (1962) Experimental clubfoot and arthrogryposis multiplex congenita. Lancet **280**: 523-526.

Filges I, Hall JG (2013) Failure to identify antenatal multiple congenital contractures and fetal akinesia - proposal of guidelines to improve diagnosis: disorders of fetal movement - proposal of guidelines. Prenat Diagn **33**: 61-74.

Franz T, Kothary R, Surani MAH, Halata Z, Grim M (1993) The Splotch mutation interferes with muscle development in the limbs. Anat Embryol (Berl) **187**: 153-160.

Henderson JH, Carter DR (2002) Mechanical induction in limb morphogenesis: the role of growth-generated strains and pressures. Bone **31**: 645-653.

Henstock JR, Rotherham M, Rose JB, El Haj AJ (2013) Cyclic hydrostatic pressure stimulates enhanced bone development in the foetal chick femur *in vitro*. Bone **53**: 468-477.

Hunziker EB (1994) Mechanism of longitudinal bone growth and its regulation by growth plate chondrocytes. Microsc Res Tech **28**: 505-519.

Kahn J, Shwartz Y, Blitz E, Krief S, Sharir A, Breitel DarioA, Rattenbach R, Relaix F, Maire P, Rountree RB, Kingsley DM, Zelzer E (2009) Muscle contraction is necessary to maintain joint progenitor cell fate. Developmental Cell **16**: 734-743.

Khatib N, Parisi C, Nowlan N (2021) Differential effect of frequency and duration of mechanical loading on fetal chick cartilage and bone development. Eur Cell Mater **41**: 531-545.

Levillain A, Rolfe R, Huang Y, Iatridis J, Nowlan N (2019) Short-term foetal immobility temporally and progressively affects chick spinal curvature and anatomy and rib development. Eur Cell Mater **37**: 23-41.

Levillain A, Ahmed S, Kaimaki D-M, Schüler S, Barros S, Labone D, Nowlan NC (2021) Prenatal muscle forces are necessary for vertebral segmentation and disc structure, but not for notochord involution in mice. Eur Cell Mater **41**: 558-575.

Meijering EHW, Niessen WJ, Viergever MA (2001) Quantitative evaluation of convolution-based methods for medical image interpolation. Med Image Anal **5**: 111-126.

Mikic B, Wong M, Chiquet M, Hunziker EB (2000) Mechanical modulation of tenascin-C and collagen-XII expression during avian synovial joint formation. J Orthop Res **18**: 406-415.

Nowlan N (2015) Biomechanics of foetal movement. Eur Cell Mater **29**: 1-21.

Nowlan NC, Bourdon C, Dumas G, Tajbakhsh S, Prendergast PJ, Murphy P (2010) Developing bones are differentially affected by compromised skeletal muscle formation. Bone **46**: 1275-1285.

Nowlan NC, Chandaria V, Sharpe J (2014) Immobilized chicks as a model system for early-onset developmental dysplasia of the hip. J Orthop Res **32**: 777-785.

Nowlan NC, Dumas G, Tajbakhsh S, Prendergast PJ, Murphy P (2012) Biophysical stimuli induced by passive movements compensate for lack of skeletal muscle during embryonic skeletogenesis. Biomech Model Mechanobiol **11**: 207-219.

Nowlan NC, Prendergast PJ, Murphy P (2008) Identification of mechanosensitive genes during embryonic bone formation. PLoS Comput Biol **4**: e1000250. DOI: 10.1371/journal.pcbi.1000250

Nowlan NC, Sharpe J (2014) Joint shape morphogenesis precedes cavitation of the developing hip joint. J Anat **224**: 482-489.

Ollion J, Cochennec J, Loll F, Escudé C, Boudier T (2013) TANGO: a generic tool for high-throughput 3D image analysis for studying nuclear organization. Bioinformatics **29**: 1840-1841.

Pacifici M, Koyama E, Iwamoto M (2005) Mechanisms of synovial joint and articular cartilage formation: recent advances, but many lingering mysteries. Birth Defects Res C Embryo Today **75**: 237-248.

Pierantoni M, Le Cann S, Sotiriou V, Ahmed S, Bodey AJ, Jerjen I, Nowlan NC, Isaksson H (2021) Muscular loading affects the 3D structure of both the mineralized rudiment and growth plate at early stages of bone formation. Bone **145**: 115849. DOI: 10.1016/j.bone.2021.115849.

Pollard AS, Boyd S, McGonnell IM, Pitsillides AA (2017) The role of embryo movement in the development of the furcula. J Anat **230**: 435-443.

Quintana L, Sharpe J (2011) Preparation of mouse embryos for optical projection tomography imaging. Cold Spring Harb Protoc **2011**: 664-669.

Roddy KA, Prendergast PJ, Murphy P (2011) Mechanical influences on morphogenesis of the knee joint revealed through morphological, molecular and computational analysis of immobilised embryos. PLoS One **6**: e17526. DOI: 10.1371/journal.pone.0017526.

Rolfe RA, Bezer JH, Kim T, Zaidon AZ, Oyen ML, Iatridis JC, Nowlan NC (2017) Abnormal fetal muscle forces result in defects in spinal curvature and alterations in vertebral segmentation and shape. J Orthop Res **35**: 2135-2144.

Schindelin J, Arganda-Carreras I, Frise E, Kaynig V, Longair M, Pietzsch T, Preibisch S, Rueden C, Saalfeld S, Schmid B, Tinevez J-Y, White DJ, Hartenstein V, Eliceiri K, Tomancak P, Cardona A (2012) Fiji: an open-source platform for biological-image analysis. Nat Methods **9**: 676-682.

Schnabel JA, Rueckert D, Quist M, Blackall JM, Castellano-Smith AD, Hartkens T, Penney GP, Hall WA, Liu H, Truwit CL, Gerritsen FA, Hill DLG, Hawkes DJ (2001) A generic framework for non-rigid registration based on non-uniform multi-level free-

form deformations. In: Medical Image Computing and Computer-Assisted Intervention - MICCAI 2001. Editors: Niessen WJ, Viergever MA. Springer Berlin Heidelberg, Berlin, Heidelberg. pp: 573-581.

Schneider CA, Rasband WS, Eliceiri KW (2012) NIH Image to ImageJ: 25 years of image analysis. Nat Methods **9**: 671-675.

Sotiriou V, Rolfe RA, Murphy P, Nowlan NC (2019) Effects of abnormal muscle forces on prenatal joint morphogenesis in mice. J Orthop Res **37**: 2287-2296.

Tan SHS, Wong KL, Lim AKS, Hui JH (2019) The earliest timing of ultrasound in screening for developmental dysplasia of the hips. Ultrasonography **38**: 321-326.

Theiler K (1989) The house mouse. Atlas of embryonic development. Springer Berlin Heidelberg, Berlin, Heidelberg. DOI: 10.1007/978-3-642-88418-4.

Web References

1. http:// gwyddion.net/ [01-09-2021]

2. https://doi.org/10.5281/zenodo.5566902 [10-10-2022]

Editor's note: There were no questions from reviewers for this paper, therefore there is no Discussion with Reviewers section. The Scientific Editor responsible for this paper was Stephen Ferguson.